Astronomy & Astrophysics manuscript no. mrk421_long_term
November 30, 2021

The relentless variability of Mrk 421 from the TeV to the radio

A. Arbet-Engels[1], D. Baack[2], M. Balbo[3], A. Biland[1], M. Blank[4], T. Bretz[1,5], K. Bruegge[2], M. Bulinski[2], J. Buss[2], M. Doerr[4], D. Dorner[4], D. Elsaesser[2], D. Hildebrand[1], K. Mannheim[4], S. A. Mueller[1], D. Neise[1], M. Noethe[2], A. Paravac[4], W. Rhode[2], B. Schleicher[4], K. Sedlaczek[2], A. Shukla[4], V. Sliusar[3]⋆, R. Walter[3]⋆, and E. von Willert[4]

[1] Department of Physics, ETH Zurich, Otto Stern Weg 5, CH-8093 Zurich, Switzerland
[2] Fakultät Physik, Technische Universität Dortmund, Otto Hahn Str. 4a, D-44227 Dortmund, Germany
[3] Department of Astronomy, University of Geneva, Chemin d'Ecogia 16, CH-1290 Versoix, Switzerland
[4] Institut für Theoretische Physik und Astrophysik, Universität Würzburg, Emil Fischer Str. 31, 97074 Würzburg, Germany
[5] Physikalisches Institut III A, RWTH Aachen University, Otto Blumenthal Str., D-52074 Aachen, Germany

Received Month Day, Year; accepted Month Day, Year.

ABSTRACT

Context. The origin of the γ-ray emission of the blazar Mrk 421 is still a matter of debate.
Aims. We used 5.5 years of unbiased observing campaign data, obtained using the FACT telescope and the Fermi LAT detector at TeV and GeV energies, the longest and densest so far, together with contemporaneous multi-wavelength observations, to characterise the variability of Mrk 421 and to constrain the underlying physical mechanisms.
Methods. We studied and correlated light curves obtained by ten different instruments and found two significant results.
Results. The TeV and X-ray light curves are very well correlated with a lag of < 0.6 days. The GeV and radio (15 Ghz band) light curves are widely and strongly correlated. Variations of the GeV light curve lead those in the radio.
Conclusions. Lepto-hadronic and purely hadronic models in the frame of shock acceleration predict proton acceleration or cooling timescales that are ruled out by the short variability timescales and delays observed in Mrk 421. Instead the observations match the predictions of leptonic models.

Key words. astroparticle physics – radiation mechanisms: non-thermal – radiative transfer – BL Lacertae objects: individual: Mrk 421

1. Introduction

Blazars are active galactic nuclei (AGNs) emitting a relativistic jet aligned with the observer's line of sight. Their spectra consist of two broad non-thermal components peaking in wavelengths from radio to optical, and in the γ-rays, respectively. If the low-energy component is very likely emitted by electron synchrotron, the origin of the high-energy component is still a matter of debate.

In some objects, including Mrk 421, the γ-ray emission is so rapidly variable that moderate Doppler boosting is inescapable during fast flares (Celotti et al. 1998). The fastest variations suggest that either a shock moves relativistically within the jet or that the emission region is much smaller than the gravitational radius and driven by interactions between stars/clouds and the jet, or by magnetic reconnection (Aharonian et al. 2017).

Mrk 421 is a high-synchrotron-peaked blazar ($z = 0.031$), with a low-energy synchrotron component peaking above 10^{17} Hz, featuring bright and persistent GeV and TeV emission with frequent flaring activities. Its average spectral energy distribution has been modelled with a one-zone leptonic synchrotron self-Compton model (SSC; Abdo et al. 2011b) or with a hadronic model where the accelerated protons cool through synchrotron emission (Cerruti et al. 2015) or interact with the leptonic synchrotron photons to create a cascade of pions and muons, decaying into γ-rays and neutrinos (Mücke & Protheroe 2001a,b).

Numerous multi-wavelength campaigns have been carried out (e.g. Tanihata et al. 2004; Aleksić et al. 2015b). During the 2009 campaign, Mrk 421 was simultaneously observed from the radio to the TeV band for 4.5 months in the absence of strong flares (Aleksić et al. 2015b). The fractional variability revealed that, despite Mrk 421 being in a relatively mild state, most variability lies in the X-ray ($F_{var} = 0.5$) and TeV ($F_{var} = 0.3$) bands. A harder-when-brighter behaviour was found in the X-rays. The smallest variations were observed in the radio. Aleksić et al. (2015b) determined a positive cross-correlation between the fluxes at keV and TeVs at zero time lag, with a maximum lag of about five days, determined from the z-transformed discrete correlation functions. Cross-correlations between optical/UV and X-rays did not show any significant correlation. While the correlation studies between TeV and keV fluxes have typically been consistent with a zero time lag, Fossati et al. (2008) reported a time lag of 2.1 ± 0.7 ks between these two bands during strong flaring activity of Mrk 421 in March 2001.

In this paper, we are using a 5.5-year observational campaign conducted on Mrk 421 at TeV energies with the First G-APD Cherenkov Telescope (FACT; Anderhub et al. 2013). These observations were not triggered (the observations were regularly scheduled independently of the source activity) and are therefore unbiased, and as regular as possible taking into account observing conditions and technical constraints. We also use continuous radio, optical, ultraviolet, X-ray, hard X-ray, and GeV light

⋆ Corresponding authors, e-mails: vitalii.sliusar@unige.ch & roland.walter@unige.ch

curves obtained quasi-simultaneously to the FACT campaign by eight additional instruments with the aim being to improve the observational constraints and compare them with the predictions of various emission models.

Section 2 describes the various instruments and data used. The multi-wavelength variability of Mrk 421 is studied in Sect. 3 and compared to model expectations in Sect. 4. Our conclusions are summarised in Sect. 5.

2. Data and analysis

To characterise the broadband variability of Mrk 421, we used data from nine different instruments spanning from the radio to the TeV and obtained between December 14, 2012, and April 18, 2018. The data and their analysis are presented in the following sections. The resulting light curves are presented in Fig. 1. The light curves obtained for FACT, Monitor of All-sky X-ray Image (MAXI), and Swift Burst Alert Telescope (Swift/BAT) include negative fluxes, as expected when the source is not detected. The Fermi Large Area Telescope (LAT) light curve is always positive because of the use of a positively defined model in the maximum-likelihood fitting. Some of the analyses presented in Sect. 3 disregard negative or low signal-to-noise-ratio ($< 2\sigma$) data points. Mrk 421 was observed at various flux states in all bands, with apparent flare duration roughly decreasing with energy (Sinha et al. 2015; Hovatta et al. 2015; Kapanadze et al. 2017). Flares observed from the X-ray to the TeV are narrow enough to be identified individually (see Table 1). At longer wavelengths the flares become wider and overlap.

2.1. FACT

FACT is an imaging atmospheric Cherenkov telescope with a 9.5 m^2 segmented mirror located at the Observatorio del Roque de los Muchachos on the island La Palma at an elevation of 2.2 km (Anderhub et al. 2013). FACT has been in operation since October 2011 and is designed to detect gamma rays with energies from hundreds of GeV up to about 10 TeV by observing the Cherenkov light produced in extensive air showers induced by gamma and cosmic rays in the Earth's atmosphere. The FACT telescope performs observations in fully remote and automatic mode. At the beginning of a shift, the telescope is started by a remote operator, usually from home. The telescope software takes over full control and monitoring of the telescope, executing the predefined schedule during the whole night of observations. In case of any problems or unfavourable weather conditions an operator is called to take appropriate action. Such an approach allows long-term regular observations of bright TeV sources at low cost. The excellent and stable performance of the camera uses silicon-based photosensors (SiPM, also known as Geiger-mode Avalanche Photo Diodes (G-APDs)) and a feedback system to keep the gain of the photosensors stable (Biland et al. 2014), which helps to maximise the duty cycle of the instrument and minimise the gaps in the light curves (Dorner et al. 2017), allowing for observation with bright ambient light. Regular operations take place with light conditions up to about 20 times brighter than the dark night conditions. Observations are typically interrupted for 4-5 days every month. The telescope can operate during full-Moon conditions (Knoetig et al. 2013).

The light curve of Mrk 421 was obtained using the Modular Analysis and Reconstruction Software (MARS, revision 19203[1]; Bretz & Dorner 2010). Thanks to the stable and homogeneous

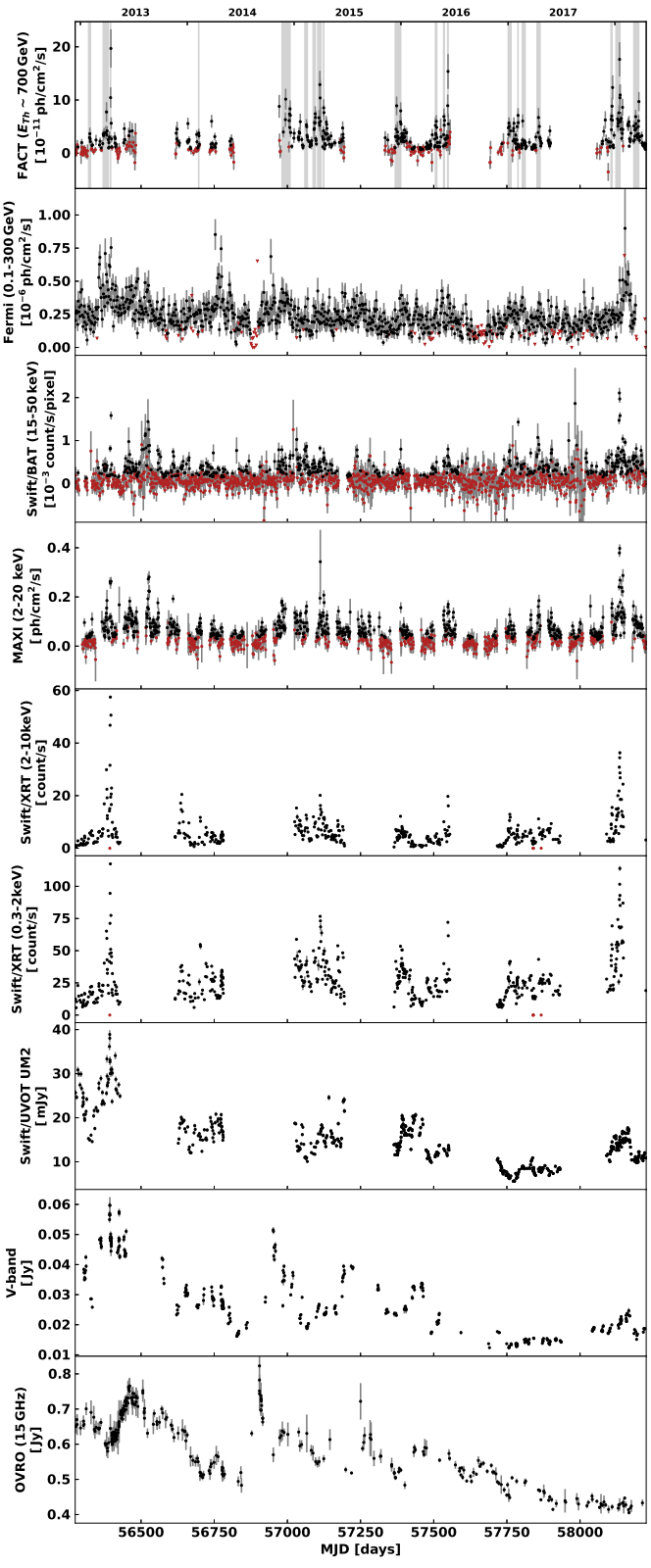

Fig. 1: Long-term light curves of Mrk 421 obtained from the radio to the TeV between December 14, 2012, and April 18, 2018. From top to bottom: FACT (E_{Th} ~ 700 GeV), Fermi LAT (0.1-300 GeV), MAXI (2-20 keV), Swift/BAT (15-50 keV), Swift/XRT (2-10 keV), Swift/XRT (0.3-2 keV), Swift/UVOT UVM2, V-band optical observations, and radio observations at 15 GHz. Flux measurement errors are denoted as vertical grey bars. Points with signal-to-noise ratio lower than two are coloured red (see Sect. 2 for details on the cleaning procedures). For the FACT light curve, there are 177 (out of 580) such points. For the Fermi LAT light curve, 95% flux upper limits (TS<25) are shown with triangles. For the FACT light curve, the flares listed in Table 1 are highlighted in grey.

[1] https://trac.fact-project.org/browser/trunk/Mars/

gain, no additional calibration is needed. After signal extraction, the images are cleaned using a two-step process. First, islands with an arrival time difference of neighbouring pixels of less than 2.4 ns are formed and adjacent islands are joined. In a second step, islands with a total signal of less than 25 pe (photon equivalents) are rejected. A principal component analysis of the remaining distribution results in a set of parameters describing the shower image. A detailed description of the data selection, reconstruction, and applied cuts for light curve and spectral extraction are provided in Beck et al. (2019). The signal from the source is determined cutting at $\theta^2 < 0.037\,\mathrm{deg}^2$, where θ is the angular distance between the reconstructed source position and the real source position in the camera plane. The source is observed in wobble-mode (Fomin et al. 1994) with a distance of 0.6 deg from the camera centre. To calculate the background, the same analysis is performed for five off-source regions, each located 0.6 deg from the camera centre. The source excess rate is derived by subtracting the scaled signal in these off-regions from the signal at the source position and dividing it by the effective exposure time.

The Crab Nebula is a standard candle at TeV energies. Even though flares have been seen at MeV/GeV energies, similar flux changes have not been found at TeV energies. Therefore, the excess rate of the Crab Nebula is used to study and correct the dependence of the excess rate from the zenith distance and trigger threshold (changed with the ambient light conditions; Bretz et al. 2013). These dependencies are similar to those of the cosmic-ray rate described in Bretz (2019) and details can be found in Beck et al. (2019). For the studied data sample, the corrections in zenith distance are less than 10% for more than 92% of the nights and in trigger threshold less than 10% for more than 72% of the nights. The maximum correction in zenith distance is 47% with only one night with a correction larger than 45%. In threshold, the largest correction is 69%, but 98% of the nights have a correction smaller than 60%. To take into account the influence of the different spectral slope of Mrk 421 compared to the Crab Nebula, the spectra of 75 time ranges between January 2013 and April 2018 determined with the Bayesian Block algorithm (see Sect. 3) were extracted (using the method described in Temme et al. (2015) and the cuts from Beck et al. (2019)) and fitted with a simple power law. Within the uncertainties, no obvious dependency was found between index and flux, and so the harder-when-brighter behaviour reported in Aleksić et al. (2015b) cannot be confirmed or rejected. The distribution of indices yields an average spectral slope of 3.35 ± 0.23, which is compatible with some previously published results of other telescopes taking into account the different energy ranges and instrument systematic errors (Albert et al. 2007). Assuming different slopes from 3.12 to 3.58, the corresponding energy thresholds and integral fluxes were determined in order to estimate the systematic error of a varying slope of the spectrum of Mrk 421. This results in a systematic flux uncertainty of less than 12% which was added quadratically to the statistical uncertainties.

For the light curve of Mrk 421, a data sample from December 14, 2012, until April 18, 2018 (MJD 56275 to 58226), has been selected applying a data-quality selection cut based on the cosmic-ray rate (Hildebrand et al. 2017). For this, the artificial trigger rate above a threshold of 750 DAC-counts, $R750$, is calculated and selected to be independent of the trigger threshold. As described in Mahlke et al. (2017) and Bretz (2019), the dependence of $R750$ on the zenith distance is determined and a corrected rate, $R750_{\mathrm{cor}}$, is calculated. To account for seasonal changes of the cosmic-ray rate due to changes in the Earth's atmosphere, a reference value, $R750_{\mathrm{ref}}$, is determined for each moon period. In a distribution of the ratio $R750_{\mathrm{cor}}/R750_{\mathrm{ref}}$, the good-quality data can be described with a Gaussian distribution. Data obtained during bad weather deviate from this. A cut is applied at the points where the distribution of the data starts deviating from the Gaussian distribution. Data with good quality are selected using a cut of $0.93 < R750_{\mathrm{cor}}/R750_{\mathrm{ref}} < 1.3$. This results in a total Mrk 421 data sample of 1628 hours of observational data of good quality. This sample contains data from 649 nights with up to 7.5 hours of observation per night. The average observation time is 2.5 hours per night. For the light curve, nights with an observation time of less than 20 minutes were rejected. The FACT light curve of Mrk 421 is presented in Fig. 1 (uppermost panel).

Systematic uncertainties can be checked by verifying the stability of the Crab Nebula, which was observed daily contemporaneously to Mrk 421. When filtered for bad weather and high night-sky background periods, the differences between the measured Crab fluxes and the reference Crab flux, when normalised by the observational uncertainties, are well represented by a Gaussian distribution.

2.2. Fermi LAT

The LAT onboard the Fermi Gamma-ray Space Telescope is the most sensitive γ-ray telescope in orbit to date. Since August 4, 2008, it has been observing the sky from 20 MeV to 300 GeV (Atwood et al. 2009) using a charged particle tracker and a calorimeter (which reach a total of 8.7 radiation length), surrounded by a segmented anti-coincidence system. Its point spread function (PSF) strongly depends on energy, reaching a 68% containment radius of $\sim 0.1^\circ$ at 40 GeV (Abdo et al. 2009). More information about the LAT is provided in Ackermann et al. (2012a) and Ackermann et al. (2012b).

For the purpose of this paper we analysed Fermi LAT data from August 4, 2008, to April 18, 2018. For the variability and correlation studies we only used the data from December 14, 2012, corresponding to the FACT observations. Data were reprocessed with the PASS8[2] pipeline and analysed using the Fermi Science Tool v10r0p5 package[3]. In order to improve the quality of the data analysis, we selected only those photons belonging to `evclass=128` and `evtype=3`, flagged with `(DATA_QUAL==1) && (LAT_CONFIG==1)`, taken while the spacecraft was outside the South Atlantic Anomaly and the source was in the field of view of the satellite. We used the `zmax=90` option in the `gtltcube` tool to minimise the background due to the atmospheric γ-rays originating from the Earth's limb.

Given the energy-dependent PSF of the instrument (Ackermann et al. 2012a), we considered only events with energy 100 MeV < E < 300 GeV, in a region of intereset (ROI) of 20° centred on Mrk 421. The fitting model, instead, included sources from the LAT four-year Point Source Catalog[4] within 25° of Mrk 421. We left the normalisation and the gamma index parameters free to vary for those sources less than 10° from the ROI centre and with a test statistic (TS) higher than 25 (corresponding to a $\sim 5\sigma$ detection) or presenting a variability index higher than 72.44, which suggests a monthly timescale variability of the source (Acero et al. 2015). We used `gll_iem_v06.fits`[5] (Acero et al.

[2] http://fermi.gsfc.nasa.gov/ssc/data/analysis/documentation/Pass8_usage.html
[3] http://fermi.gsfc.nasa.gov/ssc/data/analysis/software/
[4] http://fermi.gsfc.nasa.gov/ssc/data/access/lat/4yr_catalog/
[5] http://fermi.gsfc.nasa.gov/ssc/data/access/lat/BackgroundModels

2016) and `iso_P8R2_SOURCE_V6_v06.txt`[5] to describe the diffuse Galactic γ-ray emission and the isotropic background component, respectively.

The best fit on the entire data sample, with a power-law model described as $dN/dE = N(E/E_{\rm scale})^{-\Gamma}$, returned a normalisation of $N = (2.007 \pm 0.012) \times 10^{-11}$ ph cm^{-2} s^{-1} MeV^{-1} and a gamma index $\Gamma = 1.780 \pm 0.004$, using $E_{\rm scale} = 1187$ MeV. This implies a total integrated flux of $F_{0.1-300\ \rm GeV} = (2.10 \pm 0.02) \times 10^{-7}$ ph cm^{-2} s^{-1}. When Mrk 421 was detected with TS<25, we calculated 95% flux upper limits. Throughout this paper, we use a binning of two days, leading to upper limits for 9% of the data points (a one-day binning would lead to upper limits for 33% of the data points). Figure 1 shows the Fermi light curve. The spectral indices derived for each time bin (average 1.79 ± 0.16) do not suggest any significant spectral variability during these observations.

Using higher TS criteria to fix the parameters of the other sources yielded a difference of $\lesssim 1.8\%$ on Mrk 421 integral fluxes, and $\lesssim 0.5\%$ on the spectral index. Leaving the Galactic and isotropic normalisations free to vary or fixing them to the average ten-year value yields a final difference of $\lesssim 0.5\%$ on the integral fluxes and $\lesssim 0.03\%$ on the slope.

2.3. Swift/BAT

The wide field of view of the Swift/BAT (Krimm et al. 2013) onboard the Swift satellite allows the complete sky at hard X-rays to be monitored every few hours. For sources as bright as Mrk 421, light curves can be obtained in different energy bands with a resolution of days.

The Swift/BAT reduction pipeline is described in Tueller et al. (2010) and Baumgartner et al. (2013). Our pipeline is based on the BAT analysis software `HEASOFT` version 6.13. A first analysis was performed to derive background detector images. We created sky images (task `batsurvey`) in the eight standard energy bands (in keV: 14 - 20, 20 - 24, 24 - 35, 35 - 50, 50 - 75, 75 - 100, 100 - 150, 150 - 195) using an input catalogue of 86 bright sources that have the potential to be detected in single pointings. The detector images were then cleaned by removing the contribution of all detected sources (task `batclean`) and averaged to obtain one background image per day. The variability of the background detector images was then smoothed pixel-by-pixel fitting the daily background values with different functions (spline, polynomial). A polynomial model with an order equal to the number of months in the data set adequately represents the background variations.

The BAT image analysis was then run again using these smoothed averaged background maps. The new sky images were then stored in an all-sky pixel database by properly projecting the data onto a fixed grid of sky pixels, preserving fluxes (the angular size of the BAT pixels varies in the field of view). This database can then be used to build local images and spectra or light curves for any sky position. We compared the result of our processing to the standard results presented by the Swift team (light curves and spectra of bright sources from the Swift/BAT 70-months survey catalogue[6]) and found very good agreement.

The Swift/BAT light curves of Mrk 421 were built in several energy bands. For each time bin and energy band a weighted mosaic of the selected data is first produced and the source flux is extracted assuming fixed source position and shape of the PSF. The signal-to-noise ratio of the source varies regularly because of intrinsic variability, its position in the BAT field of view, and distance to the Sun. The 15-50 keV one-day-bin light curve presented in Fig. 1 spans from December 14, 2012, to April 18, 2018, which is over 29344 orbital periods or almost 5.5 years.

2.4. Swift/XRT

The Swift X-Ray Telescope (XRT; Burrows et al. 2005) is a sensitive (2×10^{-14} erg cm^{-2} s^{-1} in 10^4 seconds) broad-band (0.2-10 keV) X-ray imager (23.6 arcmin field of view) with an angular resolution of 18 arcsec. Its flexible scheduling allowed us to observe Mrk 421 regularly. The light curve was obtained from the online Swift-XRT products generation tool[7], which uses `HEASOFT` software version 6.22. The analysis is described in Evans et al. (2009).

2.5. MAXI

MAXI is an experiment onboard the International Space Station, observing a large part of the sky every 96 minutes and most of the sky every day. Because of its higher sensitivity and sky coverage, we used the data from the Gas Slit Camera, consisting of 12 position-sensitive large-area counters sensitive from 2 to 20 keV (Matsuoka et al. 2009).

The light curve of Mrk 421 was obtained by integrating the signal orbit by orbit (bins of 90 minutes) within a 9 square degrees region centred on the source. The background is estimated in square regions offsetted by ±3 degrees. The background-subtracted signal is normalised using the instrument response function (Isobe et al. 2010) and made publicly available[8]. The light curve of Mrk 421 was binned on daily periods. Low-significance ($< 2\sigma$) points, shown in red in Fig. 1, were discarded in the correlations studies.

2.6. Optical and ultraviolet

Mrk 421 is monitored regularly in the V band in conjunction with Fermi observations of γ-ray-bright blazars (Smith et al. 2009). The observations are carried out with the 1.54m Kuiper Telescope on Mountain Bigelow and the 2.3m Bok Telescope on Kitt Peak. For this study we used publicly[9] available data from Cycle 5 to Cycle 10 spanning from September 9, 2012, until March, 2018.

Ultraviolet fluxes from Mrk 421 are available from the Swift UltraViolet and Optical Telescope (UVOT) in three bands (UVW1, UVM2 and UVW2, Roming et al. 2005). The data were reduced with the HEASOFT package version 6.24 along with UVOT CALDB version 20170922. An aperture of 5 arcsec radius was used for the flux extraction for all bands. The background level was estimated in a circle of 15 arcsec radius located close to Mrk 421 but excluding ghost images of the bright star 51 UMa, stray light, and UVOT supporting structures.

2.7. Radio

Radio observations of Mrk 421 are performed regularly by the Owens Valley Radio Observatory (OVRO) 40 meter radio telescope as part of a blazar monitoring program (Richards et al. 2011). Observations were performed twice per week at 15 GHz (3 GHz bandwidth). The typical thermal noise reaches 4 mJy leading to a $\sim$ 3% uncertainty. The data are available from the

[6] http://swift.gsfc.nasa.gov/results/bs70mon/

[7] http://www.swift.ac.uk/user_objects/

[8] http://maxi.riken.jp/star_data/J1104+382/J1104+382.html

[9] http://james.as.arizona.edu/~psmith/Fermi/DATA/photdata.html

OVRO 40 meter telescope archive[10]. Of 329 data points, 8 with relatively large (10 − 25%) uncertainties were kept as the fractional variability and correlation analysis take these uncertainties into consideration.

3. Timing analysis

This section starts with an analysis of the variability amplitude of Mrk 421 along the spectrum, providing some interesting information and followed by a study of the light curve autocorrelations and of the significant relations and responses found across the available wavebands.

3.1. Variability

The excess variance normalised by the flux, or the fractional variability of a light curve (as proposed by Vaughan et al. 2003), can be estimated as $F_{var} = \sqrt{(S^2 - \langle\sigma_{err}^2\rangle)/\langle x\rangle^2}$ where S is the standard deviation of the light curve, $\langle\sigma_{err}^2\rangle$ is a mean squared error, and $\langle x^2\rangle$ is the average flux squared. The uncertainties on F_{var} are estimated following Poutanen et al. (2008) and Vaughan et al. (2003). As data selection (no filtering, positive flux, or data with significance above 2σ) has an effect on the fractional variability estimations (decreasing $\langle x\rangle^2$ and keeping S unchanged), we calculated F_{var} for all these cases separately.

Figure 2 features the fractional variability of Mrk 421 measured over 5.5 years across the spectrum. Similarly to previous studies (Aleksić et al. 2015b) the smallest fractional variability occurs in the radio and increases with energy up to the X-ray band. The fractional variability then drops to about 0.4 in the GeV (Fermi, 0.1-300 GeV) and rises again towards the TeVs. We verified that different light-curve binning produced the same fractional variability, and therefore the results shown in Fig. 2 represent a genuine property of Mrk 421. During previous and shorter multi-wavelength campaigns on Mrk 421 (e.g. Aleksić et al. 2015c), the fractional variability was found to be about 0.55 in the TeV band, three times lower than shown in Fig. 2. This is most likely caused by the much (10×) longer and unbiased light curves we used, which also include periods where the source is in high states. Similar F_{var} values in X-ray and TeV bands were previously also reported for short-term observations, where the source was found in a very high activity state (Acciari et al. 2020). The difference between the F_{var} values for Swift/XRT (2-10 keV) and MAXI (2-20 keV), which have partly overlapping responses, can be explained by the fact that Swift/XRT probes variations on shorter timescales.

The two maxima of the fractional variability of Mrk 421 indicate that the high-energy portions of the two emission components are more variable than the low-energy ones. In addition, Fig. 6 clearly shows that the TeV and X-ray variations are linked and simultaneous, supporting the hypothesis that a single particle population is responsible for the emission in these two distinct energy bands.

It is interesting to compare this fractional variability with that found in Mrk 501 (Ahnen et al. 2017). In Mrk 501, the fractional variability increases monotonically towards the TeV band, and reaches only about 50% of that value in the X-rays. Mrk 501 also features a lower TeV/X-rays correlation (Aleksić et al. 2015a) and a different high-energy hump spectral shape (Abdo et al. 2011a), suggesting an additional TeV emission component.

[10] http://www.astro.caltech.edu/ovroblazars/

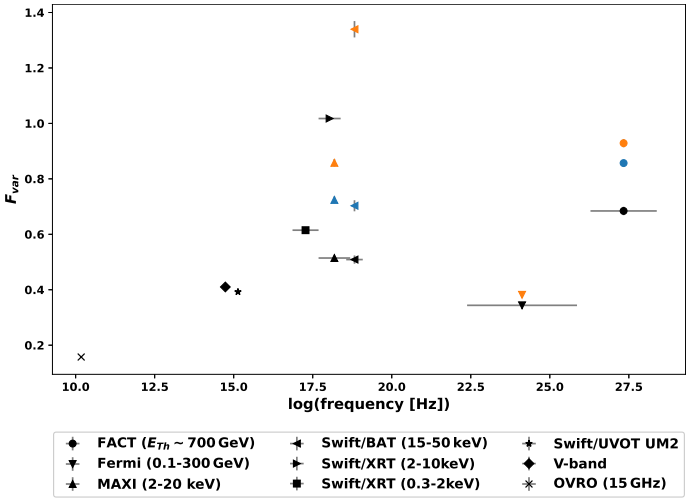

Fig. 2: Fractional variability F_{var} as a function of frequency. X-axis error bars indicate the energy band of the instrument. Y-axis error bars denote uncertainty on the F_{var} value, and are smaller than the marker for most instruments. For FACT, Fermi LAT, Swift/BAT, and MAXI, several markers are shown for different data-selection approaches: keeping all (orange), only > 2σ (black), or only positive (blue) data.

3.2. Light-curve correlations

To study the correlation between irregularly sampled light curves we used the discrete correlation function (DCF; Edelson & Krolik 1988), which allows a time resolution independent of the data sampling. Uneven time spacing of data does not allow the DCF time resolution to be decreased arbitrarily, unless long-term light curves are available, as in our case, providing enough correlation points within each time bin. We adopted one-day lag binning for the X-ray and TeV DCFs, and three-day lag binning for the DCFs involving radio, optical, and Fermi LAT light curves.

To cross check the DCF results we also calculated the Z-transformed DCF (ZDCF; Alexander 1997), which can more reliably detect correlations between sparsely time-separated data sets (each ZDCF bin has a different time width but the same number of points contributing). As our light curves are well sampled, the ZDCF did not improve the results.

We report uncertainties provided natively by the DCF. We did not use the PSRESP method (extension of the light curve; Uttley et al. 2002) to estimate the DCF uncertainties as it occasionally amplifies correlations, especially when the power spectrum is not known.

We cross-correlated all light curves with each other and found two significant and interesting cases, reported in Sects. 3.4 and 3.5. When the FWHM of the DCF peak is larger or comparable to the data sampling period, the time lags can be estimated. To obtain the lag and its uncertainty, we calculated the lag probability distribution from Monte Carlo simulations (as in Peterson et al. 1998). We generated 10^4 subsets for each pair of light curves using flux randomisation (FR) and random subset selection (RSS) processes, and calculated the resulting DCFs to obtain a representative time lag distribution using a centroid threshold of 80% of DCF maximum (Peterson et al. 2004). The lag uncertainty corresponds to the standard deviation of the distribution of the lag values obtained for the random subsets.

We performed all auto- and cross-correlations filtering out data points of low significance (<2σ in general and removing all

upper limits for Fermi/LAT), as often done in the literature (e.g. Acciari et al. 2011). By default the following figures and results are obtained with that selection. As removing periods when the source has a low significance (i.e. a low flux) can bias the results, we also performed the analyses keeping all data points (specifically mentioning these in the text). Fortunately, the final results appear very similar in the two cases.

3.3. Auto-correlations

The discrete auto-correlation function (DACF) is obtained by correlating light curves with themselves using the DCF. Following the same approach as for the cross-correlations above, we report the uncertainties as they are calculated by the DCF. The discrete auto-correlation functions of all available light curves of Mrk 421 are shown in Fig. 3, considering only $>2\sigma$ data points. A one-day DACF time binning was used for most data, excepting 5 days for GeV and 3 days for UV, optical, and radio data.

The Fermi LAT fluxes have relatively high flux uncertainties, including correlated ones (the same sky model is used for each time bin). To obtain a proper normalisation of the auto-correlation, we chose a lag step of 5 days to have unity at zero lag, as described in Edelson & Krolik (1988).

The variability timescale observed in the TeV and X-ray bands is short (of the order of the binning timescale), as expected from models where the photons in the two bands are emitted by fast cooling electrons. Longer term responses ($\sim$ 10 times the binning timescale) are observed in the GeV, optical, and radio, suggesting longer synchrotron cooling timescales at lower energies (see Sect. 4).

3.4. TeV–X-ray correlation

A strong correlation reaching 0.8 at zero lag is found between the TeV (FACT) and X-ray (Swift XRT, Swift BAT, MAXI) light curves (Fig. 4). The 1σ upper limit on the lag is of the order of 0.6 days and summing the time-lag distributions corresponding to all X-ray light curves provides a combined lag of (-0.16 ± 0.58) days (1σ) (see Fig. 5). Keeping all data points, whatever their significance, results in a combined lag of (-0.17 ± 0.48) days. The TeV/X-ray correlation was already reported using shorter and/or sparser data sets (Błażejowski et al. 2005; Aleksić et al. 2015b; Ahnen et al. 2016) providing less constraining limits on the lag. The correlation between coincident (<24h time difference) X-rays (Swift/XRT 0.3-2 keV) and TeV (FACT) fluxes can be seen in Fig. 6. These lag limits are also compatible with the results of Fossati et al. (2008) based on week-long light curves and with the assumption that X-rays and TeVs are emitted by the same population of electrons. The dispersion of the data points in Fig. 6 around the main correlation (a slope of 1.098 ± 0.033 was obtained using the orthogonal distance regression method) could be explained by intra-day variability in these bands and/or by spectral variations between flares.

As the X-ray and γ-ray flares have a typical duration that is much shorter than the observing campaign we are reporting, the TeV/X-ray cross correlation can be checked flare-by-flare. To identify statistically significant changes of state automatically, and subsequently flares, we adopt the Bayesian Block algorithm (Scargle et al. 2013). This allows us to divide the light curves into optimal blocks based on the variability statistical properties. The Bayesian Block algorithm identifies the points where the flux state is changing. The false-positive probability to define the state change was set to 1% (Scargle et al. 2013). As the Bayesian Block algorithm considers the uncertainties, the complete unfiltered light curves were used, as shown in Fig. 1. We require each

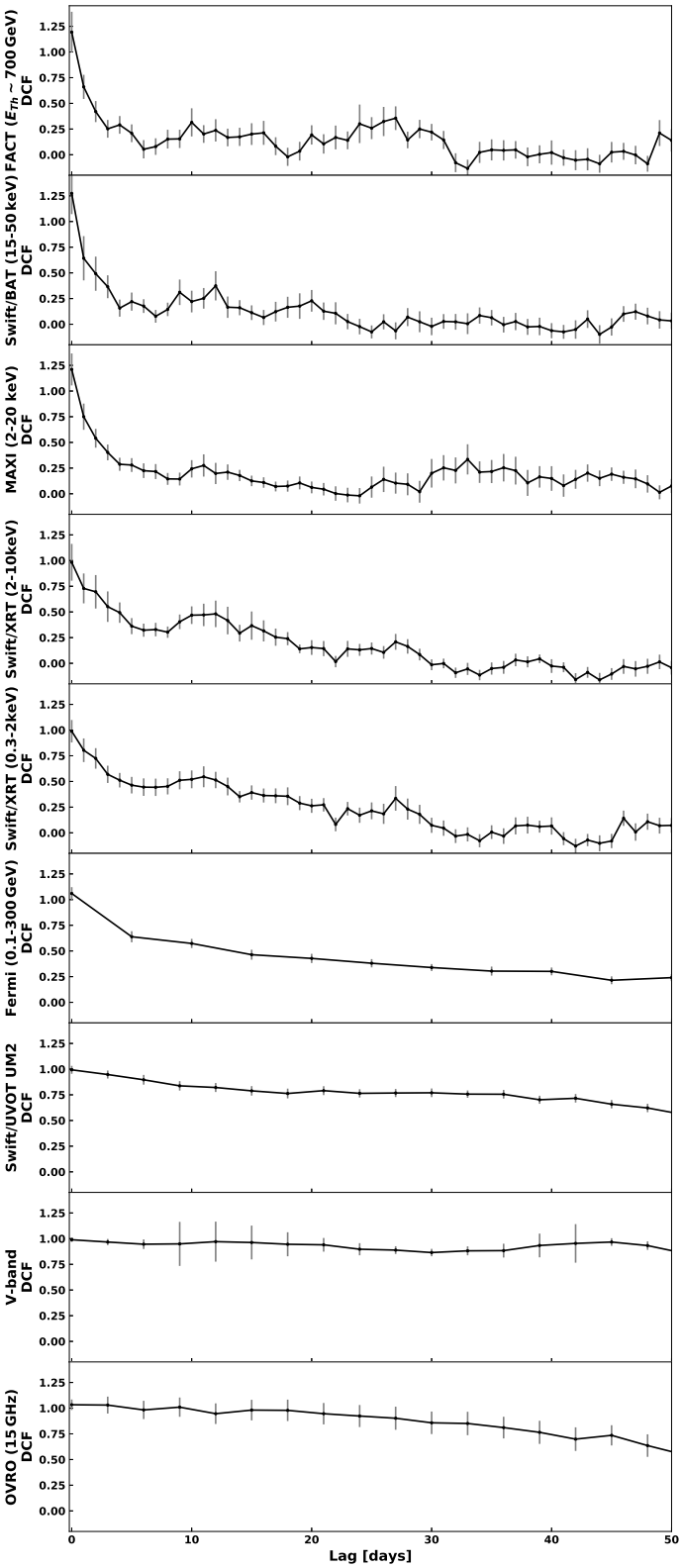

Fig. 3: Light-curve auto-correlations. From top to bottom: FACT, Swift/BAT, MAXI, Swift/XRT (2-10 keV), Swift/XRT (0.3-2 keV), Fermi LAT, Swift/UVOT UVM2, V-band, and radio. Grey error bars denote 1σ DCF uncertainties.

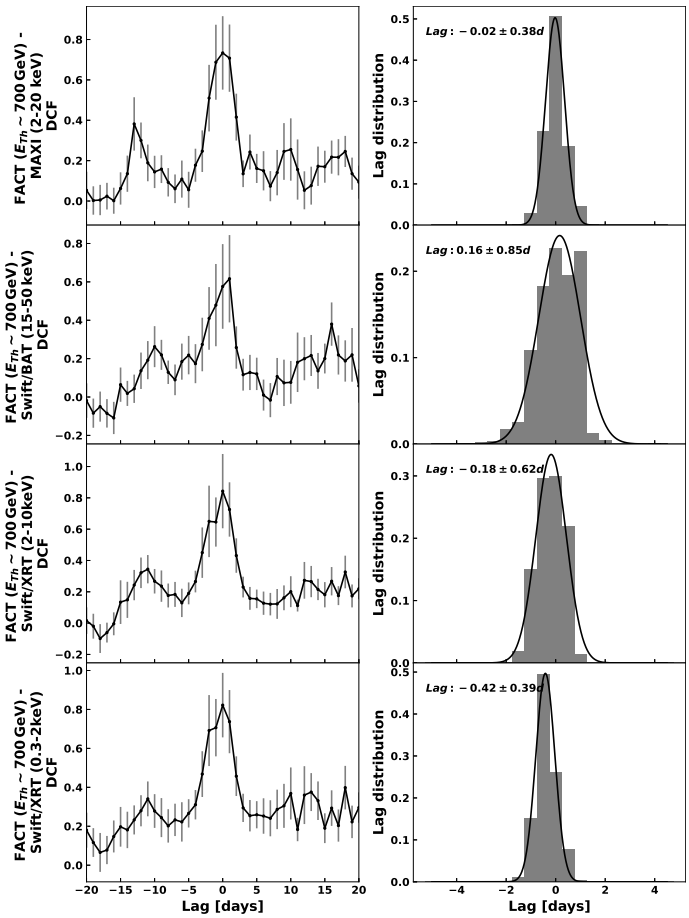

Fig. 4: DCF cross-correlations of light curves (from top to bottom panel): FACT with Swift/BAT, MAXI, Swift/XRT (2-10 keV), Swift/XRT (0.3-2 keV). One-day binning was used. Left: DCF values as a function of lag. Grey error bars denote 1σ uncertainties. Right: Lag distributions derived from FR/RSS simulations (more details are provided in Sect. 3.2). A Gaussian fit (black lines) was used to derive the lag indicated on the plots.

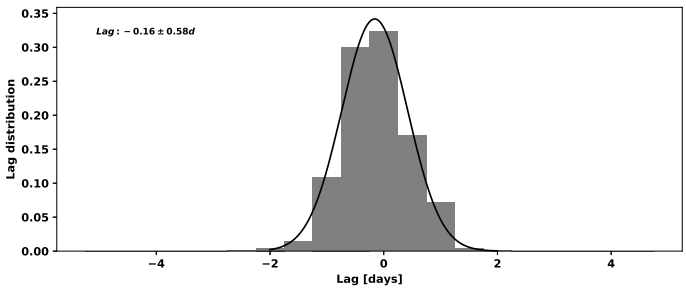

Fig. 5: Combined lag distribution between TeV and X-rays (all bands) derived from FR/RSS DCF simulations (more details are provided in Sect. 3.2). A Gaussian fit (black line) was applied to derive mean and uncertainty values.

flare to last for at least two days and have an amplitude at least 2σ above the flux in the previous block.

The Bayesian Block algorithm is sensitive to data sampling, flux variability, and flux uncertainties. As a result, the same change of the flux could be considered statistically significant or insignificant for two X-ray instruments operating simultaneously. We therefore considered all X-ray light curves and if a

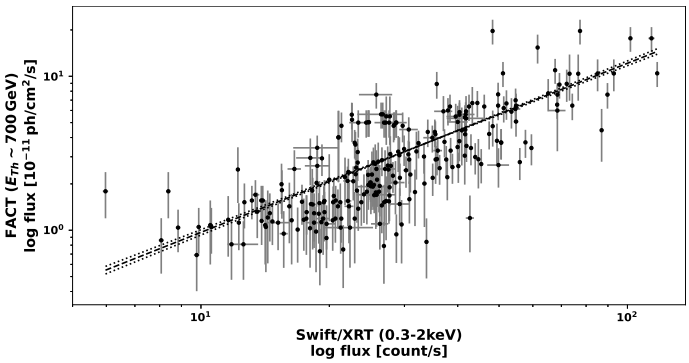

Fig. 6: TeV (FACT) and X-ray (Swift/XRT 0.3-2 keV) fluxes measured within 24 hours. The best-fit model is shown with a dashed line, and the 95% confidence region is indicated with dotted lines.

flare was detected in any of them, it was correlated to the list of TeV flares.

Out of 23 TeV flares, 22 were found to coincide with X-ray flares (Table 1). TeV and X-ray flares are of a similar duration. Removing all the low-significance ($\sigma < 2$) measurements and running the Bayesian Block algorithm again decreased the number of coincident TeV/X-ray flares from 22 to 19 and removed the TeV-only flare. The number of flares that disappeared (marked with asterisks in Table 1) is in agreement (~ 20%) with the number of low-significance data points that were removed (~ 30%).

Table 1: List of TeV flares. Flares disappearing when low-significance measurements are removed are marked with an asterisk.

Bands	Number	Time ranges, MJD
TeV only	1	56320-56328*
TeV, X-rays	22	56370-56388, 56394-56397, 56696-56698*, 56981-57010, 57059-57069, 57087-57096, 57103-57116, 57123-57125, 57368-57385, 57385-57388, 57505-57511, 57533-57537, 57547-57550, 57754-57765, 57787-57789, 57802-57813, 57853-57864, 58105-58110, 58122-58134, 58134-58137, 58183-58199*, 58199-58201*

3.5. Correlation with longer wavebands

The optical and ultraviolet light curves are highly correlated at zero lag despite their auto-correlation being wide. Both are also broadly correlated to the radio light curve (with a weaker coefficient at maximum) and are leading the radio variations by ~ 30 − 90 days at the maximum of the DCF (Fig. 7, left).

The radio light curve is broadly correlated to the GeV light curve with a lag of 30 − 100 days at the maximum of the DCF (Fig. 7, right) and is not correlated to the TeV light curve, suggesting again separate parameters controlling the variability in the GeV and TeV bands. This delay, already observed and quantified to be 40 ± 9 days by Max-Moerbeck et al. (2014) during a specific flare of Mrk 421, was interpreted as the prop-

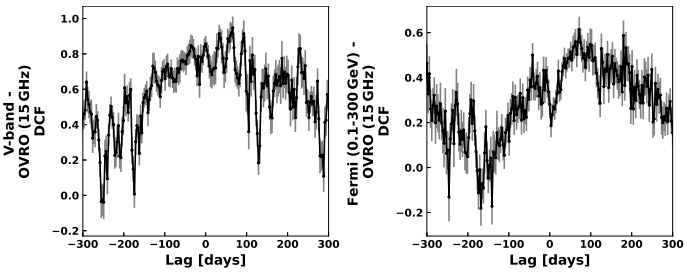

Fig. 7: Left: Cross-correlation of the V-band and radio light curves. Right: Cross-correlation of the Fermi LAT and radio light curves. The time resolution is three days. Grey error bars denote 1σ uncertainties.

agation of a shock through a conical jet. The same interpretation was proposed to explain the long-term light curves of 3C 273 (Türler et al. 1999) and in particular the radio flares corresponding to overlapping stretched and delayed GeV flares (Esposito et al. 2015).

4. Discussion

4.1. Summary of results

We performed a comprehensive study of the variability and of the correlations of multi-wavelength light curves of Mrk 421 obtained by nine different instruments over 5.5 years from December 2012 to April 2018. The fractional variability of Mrk 421 and the correlated TeV and X-ray emission are likely produced by a synchronous change of spectral shape of the low- (X-rays) and high-energy (TeV) components.

The excellent correlation at zero lag between the TeV and X-ray light curves of Mrk 421 indicates that these two emissions are driven by the same population of high-energy particles. This variability could be driven by variations of the electron maximal energy, or by for example the magnetic field that would affect both electrons and protons (Mannheim 1993). The variability of Mrk 421 is controlled, for instance, by the amplitude and the shape of the electron energy distribution, which determine the fluxes observed on the left (radio, optical, GeV) or on the right (hard X-ray, TeV) sides of the two main components of the spectral energy distribution.

4.2. Synchrotron self- or external Compton emission

Several multi-wavelength campaigns on Mrk 421 were conducted to determine the parameters of suitable SSC models from the observed spectral energy distributions (Celotti et al. 1998; Aleksić et al. 2015b; Abdo et al. 2011b; Aleksić et al. 2015c). Within the one-zone SSC model, the Doppler beaming factor δ and the magnetic field B were estimated in the ranges $21-51$ and $(3-8)\times10^{-2}$ G, respectively, with relatively high degeneracy because of the large number of parameters.

Some discrepancies were found between the observed spectra and those predicted by one-zone SSC models, especially for the Compton bump (Baloković et al. 2016; Aleksić et al. 2015b). Two-zone SSC models (Aleksić et al. 2015b) or more complex electron energy distributions (Zhu et al. 2016) have been proposed to improve the situation.

Both the analysis of very fast X-ray variations during flares (Paliya et al. 2015) and that of low velocities in the high-resolution radio jet (Blasi et al. 2013) of Mrk 421 have instead led to suggestions of a higher magnetic field $B \sim 0.5\,G$ ($\delta \sim 10$), contrasting with conclusions based on SED modelling. The cooling time for synchrotron-emitting electrons in the observer's frame of reference can be written as $t_{cool,e} \approx 15.86 \times 10^{11}\,((1+z)/\delta)^{1/2}\,(B/1\mathrm{G})^{-3/2}(\nu/1\mathrm{Hz})^{-1/2}$ seconds (Zhang et al. 2019), where B, ν, and z are respectively the magnetic field, the frequency of the observed synchrotron photons, and the source redshift.

In the high magnetic field regime ($B = 0.5\,G$ and $\delta = 10$), the synchrotron cooling timescales become 7 minutes, 89 minutes, and 16.7 hours, for 50 keV, 0.3 keV, and in the optical, respectively, roughly in agreement with the fastest variability timescale observed in Mrk 421 (Fraija et al. 2017; Paliya et al. 2015; Gaidos et al. 1996; Acciari et al. 2011). In the low magnetic field regime ($B = 0.1\,G$ and $\delta = 10$), the synchrotron cooling timescales in the observer frame become 1.2 hours and 16 hours for 50 keV and 0.3 keV, respectively, shorter than the flares that we are observing (typically 8 days, as listed in Table 8). The average delay (< 0.6 days) between the TeV and X-rays is in line with the SSC framework, where synchrotron and inverse Compton should be emitted simultaneously.

4.3. Lepto-hadronic and baryonic emission

Lepto-hadronic and baryonic models may involve different baryonic or hadronic processes to explain the high-energy emission of blazars, while the low energies remain emitted by electron synchrotron. The sychrotron–proton blazar model (Mücke & Protheroe 2001a) assumes that γ-ray photons are emitted by proton synchrotron. In Mrk 421, $\gamma_{p,max} \approx 10^{10}$, $B \approx 50$ G and $\delta \approx 20$ are required to explain the observed TeV cutoff energy (Mastichiadis et al. 2013; Abdo et al. 2011b). Synchrotron photons also interact with protons and induce pion cascades and muon synchrotron reaching energies $\gtrsim$ TeV .

In the frame of the lepto-hadronic shock acceleration models, the correlation between the TeV and the X-ray flares indicates that electrons and protons are accelerated by the same process. However the proton acceleration time of $t_{acc} = 20\,\xi\,\gamma\,m_p c/3\,eB \geq 10\,\xi$ days (where $\xi \geq 1$ is the mean free path in unit of Larmor radius, Kusunose et al. 2000; Inoue & Takahara 1996) is much longer than the delay observed between the TeV and X-ray light curves. Proton synchrotron therefore cannot be responsible for the TeV emission assuming the model parameters mentioned above (nor with smaller B and higher γ).

Muons, as secondaries of photo-protons interactions will also be generated on the proton acceleration timescales. Therefore, even if they could in principle be responsible for the TeV spectral energy distribution (Zech et al. 2017; Abdo et al. 2011b), their production timescale is also much longer than the delay observed between the X-ray and TeV variations.

Petropoulou et al. (2016) used a one-zone lepto-hadronic model to explain a 13-day flaring activity of Mrk 421 (from X-rays to TeV, including intra-day variability). The variability timescale derived by these latter authors for the electron and proton luminosities also does not correspond to the timescales mentioned above for Fermi acceleration in shocks. A different acceleration mechanism much faster than shock acceleration could be considered but this is out of the scope of the current paper.

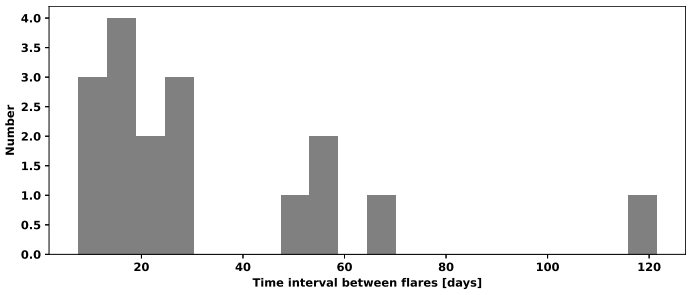

Fig. 8: Time-interval between the TeV flares listed in Table 1.

4.4. Hadronic emission

Purely hadronic models invoke proton synchrotron for the low-energy component and electron synchrotron from pion-induced cascades at higher energies ($B \approx 20$ G & $\delta \approx 16$, Mastichiadis et al. 2013). Such models were already disfavoured from the detailed study of the spectral energy distribution of Mrk 421 (Zech et al. 2017). The observed TeV variability timescale is compatible with leptonic emission but the synchrotron cooling timescale for X-ray-emitting protons in such conditions is extremely long with $t_{cool,p} \approx 1300$ years (Aharonian 2002) and even longer in the radio. Fast magneto-hydrodynamical changes could in principle explain the simultaneous X-ray and TeV correlation (as it affect all particles) but it is hard to imagine how the GeV-radio delay could be explained in this frame.

4.5. Flare timing

Falomo et al. (2002) estimated the mass of the black-hole in Mrk 421 as $10^{8.5\pm0.18} M_\odot$ from velocity dispersion measurements. The time interval Δt between FACT-detected flares shows a broad distribution peaking between 7.5 and 30 days (see Fig. 8, the periods close to 60 days could be split in half, if weak or missed flares, not listed in Table 1, are accounted for). The time interval in the source rest frame $\Delta t \cdot \delta/(1+z) \sim 10^{3-4}\ R_G/c$ (where $\delta = 10$) is comparable to that of the variations of the jet tilt (Liska et al. 2018) expected from Lense–Thirring precession (Thirring 1918) for an inclined accretion disk (Bardeen & Petterson 1975). It is therefore possible that precession induces shocks travelling down the jet.

We did not find a relation between the TeV and X-ray light curves and those at GeV and radio. One scenario that could explain this observation is the following: the TeV/X-ray emission, being produced closer to the supermassive black hole, is dominated by variations in the electron maximum energy and the inner X-ray jet viewing angle, while the GeV and radio emission, being produced further downstream in the jet, are not affected by these parameters. Magnetic turbulence seems to result in a precession angle decreasing along the jet (see Fig. 4 of Liska et al. 2018).

5. Conclusions

This analysis of the multi-wavelength light curves of Mrk 421 obtained continuously with nine different instruments over 5.5 years provides two main observational results. The strongest variations of Mrk 421 occur in the hard X-rays and in the TeVs. X-ray and TeV flares are very well correlated (all the TeV flares were detected in the X-rays). The TeV and X-ray fluxes measured simultaneously (within 24 hours) are also correlated. Thanks to the long TeV light curve provided by FACT, the average lag between the TeV and X-ray variations could be estimated as < 0.6 days (1σ). The GeV variations are strongly and widely correlated with optical and radio variability, with the latter lagging the GeV light curve by 30-100 days.

These constraints, together with the variability timescales observed in the various bands, were compared to the predictions of the three main classes of shock in jet models used to interpret the emission of blazars and of Mrk 421 in particular. Purely hadronic models are ruled out by the very long variability timescales expected in particular in the X-ray band. Lepto-hadronic models predict proton acceleration timescales, which would imply delays of $\gtrsim$10 days between the X-ray and the TeV light curves, contrasting with the upper limit on the observed lag.

Electron synchrotron self- or external Compton models do match the observational constraints but require a delay to build up between the flares observed in the GeV and in the radio. Such a delay, which has been observed also in 3C 273 and S5 0716+714, could be related to evolution of the physical conditions when shocks move along the jet. As this delay has been observed combining the complete GeV light curve, it characterises a global property of the jet and not a idiosyncrasy of a specific shock.

Acknowledgements. Author contributions: V.S. and R.W. performed the combined analysis of multi-wavelength light curves and wrote the paper. M.B. performed the Fermi LAT analysis, D.D. performed the FACT analysis, V.S. performed the Swift/UVOT analysis and R.W. performed the Swift/BAT analysis. A.A.E., A.B., T.B., D.D., K.M. & A.S. provided comments and discussed the results. All authors contributed to the construction and/or operations of the FACT telescope. The important contributions from ETH Zurich grants ETH-10.08-2 and ETH-27.12-1 as well as the funding by the Swiss SNF and the German BMBF (Verbundforschung Astro- und Astroteilchenphysik) and HAP (Helmoltz Alliance for Astroparticle Physics) to the FACT project are gratefully acknowledged. Part of this work is supported by Deutsche Forschungsgemeinschaft (DFG) within the Collaborative Research Centre SFB 876 "Providing Information by Resource-Constrained Analysis", project C3. We are thankful for the very valuable contributions from E. Lorenz, D. Renker and G. Viertel during the early phase of the FACT project. We thank the Instituto de Astrofísica de Canarias for allowing us to operate the telescope at the Observatorio del Roque de los Muchachos in La Palma, the Max-Planck-Institut für Physik for providing us with the mount of the former HEGRA CT3 telescope, and the MAGIC collaboration for their support. This research has made use of public data from the *OVRO* 40-m telescope (Richards et al. 2011), the Bok Telescope on Kitt Peak and the 1.54 m Kuiper Telescope on Mt. Bigelow (Smith et al. 2009), *MAXI* (Matsuoka et al. 2009), *Fermi* LAT (Smith et al. 2009) and *Swift* (Gehrels & Swift Team 2004). We would also like to express our gratitude to an anonymous referee.

References

Abdo, A. A., Ackermann, M., Ajello, M., et al. 2011a, ApJ, 727, 129
Abdo, A. A., Ackermann, M., Ajello, M., et al. 2009, Astroparticle Physics, 32, 193
Abdo, A. A., Ackermann, M., Ajello, M., et al. 2011b, ApJ, 736, 131
Acciari, V. A., Aliu, E., Arlen, T., et al. 2011, ApJ, 738, 25
Acciari, V. A., Ansoldi, S., Antonelli, L. A., et al. 2020, ApJS, 248, 29
Acero, F., Ackermann, M., Ajello, M., et al. 2015, ApJS, 218, 23
Acero, F., Ackermann, M., Ajello, M., et al. 2016, ApJS, 223, 26
Ackermann, M., Ajello, M., Albert, A., et al. 2012a, ApJS, 203, 4
Ackermann, M., Ajello, M., Allafort, A., et al. 2012b, Astroparticle Physics, 35, 346
Aharonian, F. A. 2002, MNRAS, 332, 215
Aharonian, F. A., Barkov, M. V., & Khangulyan, D. 2017, ApJ, 841, 61
Ahnen, M. L., Ansoldi, S., Antonelli, L. A., et al. 2016, A&A, 593, A91
Ahnen, M. L., Ansoldi, S., Antonelli, L. A., et al. 2017, A&A, 603, A31
Albert, J., Aliu, E., Anderhub, H., et al. 2007, ApJ, 663, 125
Aleksić, J., Ansoldi, S., Antonelli, L. A., et al. 2015a, A&A, 573, A50
Aleksić, J., Ansoldi, S., Antonelli, L. A., et al. 2015b, A&A, 576, A126
Aleksić, J., Ansoldi, S., Antonelli, L. A., et al. 2015c, A&A, 578, A22
Alexander, T. 1997, in Astrophysics and Space Science Library, Vol. 218, Astronomical Time Series, ed. D. Maoz, A. Sternberg, & E. M. Leibowitz, 163

Anderhub, H., Backes, M., Biland, A., et al. 2013, Journal of Instrumentation, 8, P06008
Atwood, W. B., Abdo, A. A., Ackermann, M., et al. 2009, ApJ, 697, 1071
Baloković, M., Paneque, D., Madejski, G., et al. 2016, ApJ, 819, 156
Bardeen, J. M. & Petterson, J. A. 1975, ApJ, 195, L65
Baumgartner, W. H., Tueller, J., Markwardt, C. B., et al. 2013, ApJS, 207, 19
Beck, M., Arbet-Engels, A., Baack, D., et al. 2019, 36, 630
Biland, A., Bretz, T., Buß, J., et al. 2014, Journal of Instrumentation, 9, P10012
Blasi, M. G., Lico, R., Giroletti, M., et al. 2013, A&A, 559, A75
Błażejowski, M., Blaylock, G., Bond, I. H., et al. 2005, ApJ, 630, 130
Bretz, T. 2019, Astroparticle Physics, 111, 72
Bretz, T., Biland, A., Buß, J., et al. 2013, arXiv e-prints [arXiv:1308.1516]
Bretz, T. & Dorner, D. 2010, in Astroparticle, Particle and Space Physics, Detectors and Medical Physics Applications, ed. C. Leroy, P.-G. Rancoita, M. Barone, A. Gaddi, L. Price, & R. Ruchti, 681–687
Burrows, D. N., Hill, J. E., Nousek, J. A., et al. 2005, Space Sci. Rev., 120, 165
Celotti, A., Fabian, A. C., & Rees, M. J. 1998, MNRAS, 293, 239
Cerruti, M., Zech, A., Boisson, C., & Inoue, S. 2015, MNRAS, 448, 910
Dorner, D., Adam, J., Ahnen, L. M., et al. 2017, International Cosmic Ray Conference, 35, 609
Edelson, R. A. & Krolik, J. H. 1988, ApJ, 333, 646
Esposito, V., Walter, R., Jean, P., et al. 2015, A&A, 576, A122
Evans, P. A., Beardmore, A. P., Page, K. L., et al. 2009, MNRAS, 397, 1177
Falomo, R., Kotilainen, J. K., & Treves, A. 2002, The Astrophysical Journal, 569, L35
Fomin, V. P., Stepanian, A. A., Lamb, R. C., et al. 1994, Astroparticle Physics, 2, 137
Fossati, G., Buckley, J. H., Bond, I. H., et al. 2008, ApJ, 677, 906
Fraija, N., Benítez, E., Hiriart, D., et al. 2017, ApJS, 232, 7
Gaidos, J. A., Akerlof, C. W., Biller, S., et al. 1996, Nature, 383, 319
Gehrels, N. & Swift Team. 2004, New Astronomy Reviews, 48, 431
Hildebrand, D., Ahnen, M. L., Balbo, M., et al. 2017, International Cosmic Ray Conference, 35, 779
Hovatta, T., Petropoulou, M., Richards, J. L., et al. 2015, MNRAS, 448, 3121
Inoue, S. & Takahara, F. 1996, ApJ, 463, 555
Isobe, N., Sugimori, K., Kawai, N., et al. 2010, PASJ, 62, L55
Kapanadze, B., Dorner, D., Romano, P., et al. 2017, ApJ, 848, 103
Knoetig, M. L., Biland, A., Bretz, T., et al. 2013, in International Cosmic Ray Conference, Vol. 33, International Cosmic Ray Conference, 1132
Krimm, H. A., Holland, S. T., Corbet, R. H. D., et al. 2013, The Astrophysical Journal Supplement Series, 209, 14
Kusunose, M., Takahara, F., & Li, H. 2000, ApJ, 536, 299
Liska, M., Hesp, C., Tchekhovskoy, A., et al. 2018, MNRAS, 474, L81
Mahlke, M., Bretz, T., Adam, J., et al. 2017, International Cosmic Ray Conference, 35, 612
Mannheim, K. 1993, A&A, 269, 67
Mastichiadis, A., Petropoulou, M., & Dimitrakoudis, S. 2013, MNRAS, 434, 2684
Matsuoka, M., Kawasaki, K., Ueno, S., et al. 2009, PASJ, 61, 999
Max-Moerbeck, W., Hovatta, T., Richards, J. L., et al. 2014, MNRAS, 445, 428
Mücke, A. & Protheroe, R. J. 2001a, Astroparticle Physics, 15, 121
Mücke, A. & Protheroe, R. J. 2001b, International Cosmic Ray Conference, 3, 1153
Paliya, V. S., Böttcher, M., Diltz, C., et al. 2015, ApJ, 811, 143
Peterson, B. M., Ferrarese, L., Gilbert, K. M., et al. 2004, ApJ, 613, 682
Peterson, B. M., Wanders, I., Horne, K., et al. 1998, PASP, 110, 660
Petropoulou, M., Coenders, S., & Dimitrakoudis, S. 2016, Astroparticle Physics, 80, 115
Poutanen, J., Zdziarski, A. A., & Ibragimov, A. 2008, MNRAS, 389, 1427
Richards, J. L., Max-Moerbeck, W., Pavlidou, V., et al. 2011, ApJS, 194, 29
Roming, P. W. A., Kennedy, T. E., Mason, K. O., et al. 2005, Space Sci. Rev., 120, 95
Scargle, J. D., Norris, J. P., Jackson, B., & Chiang, J. 2013, ApJ, 764, 167
Sinha, A., Shukla, A., Misra, R., et al. 2015, A&A, 580, A100
Smith, P. S., Montiel, E., Rightley, S., et al. 2009, arXiv e-prints [arXiv:0912.3621]
Tanihata, C., Kataoka, J., Takahashi, T., & Madejski, G. M. 2004, ApJ, 601, 759
Temme, F., Ahnen, M. L., Balbo, M., et al. 2015, in International Cosmic Ray Conference, Vol. 34, 34th International Cosmic Ray Conference (ICRC2015), 707
Thirring, H. 1918, Physikalische Zeitschrift, 19, 33
Tueller, J., Baumgartner, W. H., Markwardt, C. B., et al. 2010, ApJS, 186, 378
Türler, M., Courvoisier, T. J.-L., & Paltani, S. 1999, A&A, 349, 45
Uttley, P., McHardy, I. M., & Papadakis, I. E. 2002, MNRAS, 332, 231
Vaughan, S., Edelson, R., Warwick, R. S., & Uttley, P. 2003, MNRAS, 345, 1271
Zech, A., Cerruti, M., & Mazin, D. 2017, A&A, 602, A25
Zhang, Z., Gupta, A. C., Gaur, H., et al. 2019, ApJ, 884, 125
Zhu, Q., Yan, D., Zhang, P., et al. 2016, MNRAS, 463, 4481